CO_2 saturation estimates at Sleipner (North Sea) from seismic tomography and rock physics inversion

Hong Yan [1, 2], Bastien Dupuy [1], Anouar Romdhane [1], Børge Arntsen [2]

[1]Affiliation: SINTEF Industry

[2]Affiliation: Department of Geosciences and Petroleum, NTNU

Email: bastien.dupuy@sintef.no, anouar.romdhane@sintef.no, borge.arntsen@ntnu.no, myahongyan@outlook.com.

Abstract

CO_2 saturations are estimated at Sleipner using a two-step imaging workflow. The workflow combines seismic tomography (full-waveform inversion) and rock physics inversion and is applied to a 2D seismic line located near the injection point at Sleipner. We use baseline data (1994 vintage, before CO_2 injection) and monitor data which was acquired after 12 years of CO_2 injection (2008 vintage). P-wave velocity models are generated using the Full-Waveform Inversion (FWI) technology and then, we invert selected rock physics parameters using a Rock Physics Inversion (RPI) methodology. FWI provides high-resolution P-wave velocity models both for baseline and monitor data. The physical relations between rock physics properties and acoustic wave velocities in the Utsira unconsolidated sandstone (reservoir formation) are defined using a dynamic rock physics model based on well-known Biot-Gassmann theories. For data prior to injection, rock frame properties (porosity, bulk, and shear dry moduli) are estimated using RPI which allows deriving physically-consistent properties with related uncertainty. We show that the uncertainty related to limited input data (only P-wave velocity) is not an issue because the mean values of parameters are correct. These rock frame properties are then used as a priori constraint in the monitor case. For monitor data, the FWI results show nicely resolved thin layers of CO_2-brine saturated sandstones under intra-reservoir shale layers. The CO_2 saturation estimation is carried out by plugging an effective fluid phase in the rock physics model. Calculating the effective fluid bulk modulus of the brine-CO_2 mixture (using Brie equation in our study) is shown to be the key factor to link P-wave velocity to CO_2 saturation. The inversion tests are done with several values of Brie/patchiness exponent and show that the CO_2 saturation estimates are varying between 0.30 to 0.90 depending on the rock physics model and the location in the reservoir. The uncertainty in CO_2 saturation estimation is usually lower than 0.20. When the patchiness exponent is considered as unknown, the inversion

is less constrained and we end up with values of exponent varying between 5 and 20 and up to 33 in the specific reservoir area. These estimations tend to show that the CO_2-brine mixing is between uniform and patchy mixing and variable throughout the reservoir.

Introduction

The global warming is gaining lots of attention in the last decade with the increasing energy demand and fossil energy consumption. Excessive CO_2 emissions which have a substantial contribution to the global warming (Metz et al. 2005) require the implementation of immediate mitigation measures. The CO_2 Capture and Storage (CCS) technology is hence proposed as a mean to reduce the CO_2 emission into the atmosphere. Large CO_2 storage capacity has already been proven in deep saline aquifers (Halland et al. 2011, Böhm et al. 2015). The Sleipner CO_2 storage site is the first commercial-scale offshore storage operation and the longest in operation in the world. Geophysical monitoring (including seismic and non-seismic techniques) is used to monitor the subsurface changes related to the CO_2 plume migration, in order to verify conformance and early detection of potential leakage (containment monitoring).

The seismic monitoring programme at Sleipner includes a 3D baseline survey prior to CO_2 injection and several monitor surveys every two to three years (Arts et al. 2008, Furre et al. 2015, Furre et al. 2017). Previous studies based on time-lapse analysis help to reveal the details of the CO_2 plume development (Arts et al. 2004, Arts et al. 2002, Eiken et al. 2000). Structural mapping and frequency decomposition have been used to estimate the upper most layer thickness (White 2013, Williams and Chadwick 2012). Arts et al. (2002) give quantitative estimates of CO_2 mass using amplitude information. More recently, Furre et al. (2015) perform a detailed analysis of the thin CO_2 layers, with respect to time shift development and amplitude changes.

The proper understanding of saturation development in Utsira sandstone has been widely studied by several authors. Ghaderi and Landrø (2009) use seismic modeling of thin layer responses and propose a simultaneous inversion of velocity and layer thicknesses of partially saturated layers with CO_2. Post-stack impedance analysis (Ghosh et al. 2015) and time-lapse

AVO analysis (Chadwick et al. 2010) have been applied to estimate CO_2 saturations. Bergmann and Chadwick (2015) propose a method using time-shift analysis to estimate the influence of fluid mixing law both with synthetic and real data. As an alternative, quantitative maps of velocity properties derived at Sleipner using full waveform inversion have been used as input to estimate saturation distributions. Queiber and Singh (2013) and Romdhane and Querendez (2014) apply FWI in order to derive highly resolved P-wave velocity models. Queiber and Singh (2013) use simple rock physics relations (Gassmann (1951) model combined with Brie's law (Brie et al. 1995)) to describe the CO_2 and brine mixture from the P-wave velocity. Dupuy et al. (2016) propose a two-step workflow with dynamic rock physics models to tackle the existing limitation in frequency sensitivity and obtain reliable reservoir properties from high-resolution velocity models. Sensitivity studies have highlighted that extra input data in the inversion process, such as shear wave velocity and P-wave quality factors are important for the estimation of rock frame moduli and can be helpful to better constrain in the estimation of CO_2 saturation (Dupuy et al. 2016, Dupuy et al. 2017, Böhm et al. 2015). At Sleipner, (Dupuy et al. 2017) shows however that the estimation of CO_2 saturations from P-wave velocity models derived from FWI is still possible.

In this work, FWI is combined with the rock physics inversion method to invert for selected poroelastic properties (rock frame moduli, porosity, CO_2 saturation and Brie patchiness exponent) and to derive high-resolution maps of CO_2 saturation with uncertainty. Data from 1994 and 2008 vintages are used. The rock frame properties are recovered using baseline data and used as a priori parameters to estimate CO_2 saturation distribution with the monitor dataset. We invert the CO_2 saturation and other properties for the monitor case and we constrain the inversion using a priori geological information (fluid properties, grain properties, permeability, and cementation factor) and a priori information derived from the baseline results (bulk

modulus, shear modulus, and porosity). We also analyze how the Brie exponent, describing the fluids distribution (from uniform to patchy mixing), is affecting the results.

This paper is divided into four sections. While the first part gives a description of the methodology, the second section gives a short description of the geological context at Sleipner justifying the choice of some a priori parameters. The results for both baseline and monitor data are described in section 3. Section 4 discusses the obtained results and compares them to other studies.

Methodology

We use a two-step workflow combining FWI and RPI methods. From FWI, we generate a P-wave velocity model that is used as input of the rock physics inversion step.

FWI is performed in the frequency-space domain (Pratt et al. (1998)). The 2D acoustic wave equation is solved using finite differences with the mixed grid approach (Hustedt et al. 2004). The inverse problem is solved using a pre-conditioned gradient algorithm. The gradient method in its standard form provides a relationship between the perturbation model and the data residuals. An approximation of the Hessian operator with only the diagonal elements is used to save computation cost. Basic data preprocessing steps (including extracting guns, muting, coordinate transformation) are performed before running the inversion (Romdhane and Querendez (2014)). We derive an initial P-wave velocity model using RMS velocity in time converted into interval velocity in depth. The misfit function and the gradient of the misfit at iteration *n* can be expressed:

$$\begin{aligned} \xi(\mathbf{m}) &= \frac{1}{2}\left\|\mathbf{d}_{\mathrm{mod}} - \mathbf{d}_{obs}\right\|^2, \\ \frac{\partial \xi(\mathbf{m}_n)}{\partial \mathbf{m}} &= \Re \mathrm{e}\left\{\mathbf{J}^T \delta \mathbf{d}^*\right\}. \end{aligned} \tag{1}$$

Where $\frac{\partial \xi(\mathbf{m}_n)}{\partial \mathbf{m}}$ is the gradient of the misfit at iteration *n*. $\mathbf{d}_{\text{mod}}$ and $\mathbf{d}_{obs}$ are the modeled and observed data, respectively. $\Re \mathrm{e}$ is the real part of a complex number. $\mathbf{J}$ denotes the Jacobian matrix, thus $\mathbf{J}^T$ is the transpose of the Jacobian matrix. $\delta \mathbf{d}^*$ denotes the conjugate of the data residuals. The perturbation model is given by:

$$\delta \mathbf{m}_n = \mathbf{m}_{n+1} - \mathbf{m}_n. \tag{2}$$

The gradient method can be formulated as the link between the perturbation model and data residuals, and is given as:

$$\delta \mathbf{m}_n = -\alpha_n \frac{\partial \xi(\mathbf{m}_n)}{\partial \mathbf{m}}. \tag{3}$$

Where α_n is the step length at iteration *n*. Proper scaling and regularization can be applied to ensure the computational stability. The approximate Hessian $\mathbf{H}_a$ can be written:

$$\mathbf{H}_a = \Re e\left\{\mathbf{J}^T \mathbf{J}^*\right\}. \tag{4}$$

If we only consider the diagonal term of the approximate Hessian, the model update at iteration *n* becomes:

$$\delta \mathbf{m}_n = -\alpha_n (diag \mathbf{H}_{a_n} + \lambda \mathbf{I})^{-1} \frac{\partial \xi(\mathbf{m}_n)}{\partial \mathbf{m}}. \tag{5}$$

Where λ denotes a damping parameter used to ensure computational stability.

The second step consists in solving the inverse problem linking seismic properties and rock physics properties. The link between rock physics parameters and seismic attributes constitutes the forward problem, usually called the rock physics model. The forward problem can be

described in a generic manner by Biot-Gassmann theory (Biot 1956a, Gassmann 1951) as long as rock frame properties are somehow defined or estimated.

The Biot-Gassmann equations are valid under several assumptions. The Gassmann equations are valid within a low frequency limit and do not account for the chemical interaction between the grains and the fluid phases. The Biot theory is limited to homogeneous and isotropic media, which consists of only one type of grain. To be more realistic, Pride (2005) extended the Biot-Gassmann equations and included a generalized dynamic permeability (Johnson et al. 1987). The extensive Biot-Gassmann theory can be applied to a multi-composite material saturated with a multi-fluid mixture using averaging techniques. In addition, this approach is valid within a wide frequency range. More details on the assumptions and theory for this rock physics model are given in Pride (2005). The extensive Biot-Gassmann equations allow us to calculate the viscoelastic attributes for an effective fluid phase even if only P-wave velocity is used

Biot (Biot 1956b) demonstrates that there are three types of waves propagating in a fluid saturated porous medium. These are compressional wave (P-wave), shear wave (S-wave), and an additional slow compressional wave (Biot wave or slow P-wave). The slowness of P wave is formulated by Pride (2005) as:

$$S_P^2(\omega) = \frac{\gamma(\omega)}{2} - \frac{1}{2}\sqrt{\gamma^2(\omega) - \frac{4(\rho\mathring{\rho}(\omega) - \rho_f^2)}{HM - C^2}}. \tag{6}$$

Thus, we can deduce the effective P-wave velocity as:

$$V_p(\omega) = \frac{1}{\mathrm{Re}\left(S_p(\omega)\right)}. \tag{7}$$

In equations (6), ρ and ρ_f and $\tilde{\rho}(\omega)$ are bulk density, effective fluid density, and flow resistance term. Note that ω is the complex pulsation and is involved in frequency-dependent terms such as $\tilde{\rho}(\omega)$ and $\gamma(\omega)$. The undrained bulk modulus K_U, the Biot modulus C, the shear modulus G and the fluid storage coefficient M are the four mechanical moduli. The additional terms $\gamma(\omega)$ and H are defined by:

$$\begin{aligned} \gamma(\omega) &= \frac{\rho M + \tilde{\rho}(\omega) H - 2\rho_f C}{HM - C^2}, \\ H &= K_U + \frac{4}{3}G. \end{aligned} \tag{8}$$

The four mechanical moduli are related to the homogenized porous solid. K_U, C, and M are formulated as:

$$\begin{aligned} K_U &= \frac{\phi K_d + (1-(1+\phi)K_d / K_s)K_f}{\phi(1+\Delta)}, \\ C &= \frac{(1-K_d / K_s)K_f}{\phi(1+\Delta)}, \\ M &= \frac{K_f}{\phi(1+\Delta)}. \end{aligned} \tag{9}$$

Where the term Δ is given by:

$$\Delta = \frac{1-\phi}{\phi}\frac{K_f}{K_s}\left(1 - \frac{K_d}{(1-\phi)K_s}\right). \tag{10}$$

Where porosity ϕ is defined as the ratio between void and total volume in the solid matrix. K_d, G_d, K_s, and K_f are respectively the frame bulk modulus, frame shear modulus, the grains bulk modulus and the effective fluid bulk modulus.

We consider the solid material for both shale and sand layers consists of a mix of clay and quartz grains. We compute the grains bulk moduli K_S by averaging the bounds (Hashin and Shtrikman 1963). The grain density ρ_S is computed using an arithmetic average:

$$\rho = (1-\phi)\rho_s + \phi\rho_f \,. \tag{11}$$

The extended Biot-Gassmann formulation given by Pride (2005) is valid over a wide range of frequency because it involves Johnson et al. (1987) model who gives a frequency dependent dynamic permeability $k(\omega)$. It allows for correcting the seismic permeability and differentiate the viscous and inertial predominant effects at low and high frequency domain (Dupuy et al. 2016). The dynamic permeability $k(\omega)$ is expressed by Johnson et al. (1987):

$$k(\omega) = \frac{k_0}{\sqrt{1-\frac{1}{2}i\frac{\omega}{\omega_c}} - i\frac{\omega}{\omega_c}} \,. \tag{12}$$

Where ω is the angular frequency. ω_c is the characteristic angular frequency which characterizes the maximum attenuation peak. k_0 is the hydraulic permeability. The characteristic frequency ω_c can be formulated with the cementation factor m, the effective fluid viscosity η and the effective fluid density ρ_f (Adler et al. 1992) such as:

$$\omega_c = \frac{\eta}{\rho_f k_0 \phi^{-m}} \,. \tag{13}$$

Then, we can define frequency dependent flow resistance term $\beta(\omega)$ which is involved in the slowness equation (6) and is defined by:

$$\beta(\omega) = \frac{i\eta}{\omega k(\omega)} \,. \tag{14}$$

Where i denotes the complex number.

For the monitor step, it is assumed that the fluid phase in the pore space can be treated as a single-phase mixture of brine and CO_2, with effective properties computed using Brie mixing law (Brie et al. 1995) for fluid bulk modulus, Teja & Rice equation (Teja and Rice 1981) for effective viscosity, and arithmetic average (Voigt 1928) for fluid density. The sensitivity tests provided in Dupuy et al. (2016) show that the fluid bulk modulus is the main factor affecting the P-wave velocity change. The Brie equation involves an empirical exponent e:

$$K_f = (K_{CO2} - K_W)S_W^e + K_{CO2}, \tag{15}$$

where S_W denotes the brine saturation, K_{CO2} and K_W denote the CO_2 and brine bulk moduli, respectively. The exponent e can vary between 1 and 40 (Brie et al. 1995), which corresponds to various mixture trends (Figure 1). For instance, the lower bound (e=40) stands for the so-called uniform mixing (the two fluids are mixed at the finest scale), while the upper bound (e=1) stands for the so-called patchy mixing. It is worth noting that the patchy mixing is related to empirical observations and its definition is variable depending on the authors. The exponent e is proposed to be 3 (Brie et al. 1995) and 5 (Carcione and Picotti 2006) to match the case related to gas and brine mixture. The Brie exponent e is sometimes called patchiness exponent (Papageorgiou et al. 2016). The set of rock physics model equations (6-14) constitute the forward model that allows us to compute visco-elastic attributes (mainly P-wave velocity) from rock physics properties (solid and fluid phases and rock frame properties).

To solve the rock physics inversion problem, we use a semi-global optimization method (Neighborhood Algorithm (NA) (Sambridge 1999)) to minimize the discrepancy between observed data and calculated data obtained by forward modeling. The method searches for the global minimum over the whole model space in a partially random way and the search process

is guided by each iteration towards areas with a lower misfit. The scalar misfit function $C(\mathbf{m})$ between the observed data $\mathbf{d}_{\mathbf{obs}}$ and the estimated data $g(\mathbf{m})$ from the forward modeling can be given as an L_2 norm:

$$C(\mathbf{m}) = \left[(\mathbf{d}_{\mathbf{obs}} - g(\mathbf{m}))^T (\mathbf{d}_{\mathbf{obs}} - g(\mathbf{m})) \right]. \quad (16)$$

The NA algorithm has only two control parameters: the number of new models at each iteration and the resampling size of Voronoï cells. The misfit of the previous iteration decides the new sampling of Voronoï cell for the next iteration. Sambridge (1999) and Dupuy et al. (2016) provide more details on the NA algorithm and the rock physics inversion, respectively.

The rock physics inversion process give estimates of selected parameters with the related uncertainty. The sensitivity study by (Dupuy et al. 2017) shows that the estimation of CO_2 saturation from P-wave velocity input only is not well constrained when the CO_2 saturation is high (it is directly related to the shape of the P-wave velocity versus saturation curve, see Figure 1). Examples of the misfit function shapes for the estimation of frame parameters and saturation are given in sensitivity tests. By assuming a Gaussian distribution of estimated models, we can estimate the mean value and associated standard deviation to assess the uncertainty.

Geological background

Since 1996, about 0.9 million tons of CO_2 is annually injected into the Utsira formation at Sleipner at a depth of 1012 m below the sea level through a deviated well (Arts et al. 2008). The thickness of the Utsira sandstone is about 300 m and is surrounded by the Nordland shale on the top and the Hordaland shale on the bottom. The caprock is assumed to be a good quality seal with a low probability of leakage (Chadwick et al. 2004). The Utsira formation consists of late Miocene to early Pliocene dominantly sandy unit and some shaly intra-reservoir horizons

(Chadwick et al. 2000). It is a highly porous, unconsolidated, permeable sandstone which shows good reservoir properties for high injection rate through only one single well (Michael et al. 2010). The intra-reservoir shale layers are very thin and can be less than 1 m thick Zweigel (2000).

To constrain our rock physics inversion, we need to determine a set of realistic a priori rock physics properties. These parameters are defined based on the existing geological studies on Sleipner field. Grain moduli K_s of the Utsira sandstone and the Nordland shale are calculated by the Hashin-Shtrikman bounds method (Mavko et al. 2009, Hashin and Shtrikman 1963). Grain density ρ_S for the Utsira sandstone and the Nordland shale are computed using volume weighted averages. The cementation parameter m (Pride 2005) is assumed to be equal to 1 for the unconsolidated sandstone and mudstone. As discussed in sensitivity tests by Dupuy et al. (2016), the cementation factor has a negligible influence on P-wave velocity. The permeability for the Utsira formation is high and ranges from 1×10^{-12} m^2 to 3×10^{-12} m^2 (Boait et al. 2012). We use an average permeability of 2×10^{-12} m^2 for Utsira formation. The permeability of Nordland shale is defined from lab data and assumed to be equal to 1.48×10^{-17} m^2. The grains and rock frame properties of Utsira sandstone and Nordland shale are given in Table 1.

We consider a CO_2 and brine mixture after CO_2 injection and a fully brine saturated medium before CO_2 injection for the saturating fluids properties. The bulk modulus of brine is equal to 2.3 GPa at reservoir conditions (Boait et al. 2012), and the density of brine is assumed to be equal to 1030 kg/m^3 (Mavko et al. 2009) at reservoir temperature and pressure. Most of the CO_2 is stored in a supercritical state (Arts et al. 2008) and we use a relatively high density of 700 kg/m^3 for the CO_2 phase (Lindeberg 2013). Since the initial pore pressure of 8 MPa is considered (Furre and Eiken 2014) and the reservoir temperature is ranging between 27 (top Utsira formation) and 37℃ (near injection point), the range of K_{CO2} is estimated to be equal to

0.02 GPa to 0.075 GPa (Ghaderi and Landrø 2009). We use a value of 0.075 GPa for bulk modulus of CO_2 (Lindeberg 2013) regarding in-situ pressure and temperature conditions. The viscosity of CO_2 is discussed in many papers and depends on the temperature and pressure (Gasda et al. 2012, Singh et al. 2010). However, the effective viscosity influence on seismic velocity is minor at low frequency (Dupuy and Stovas 2016). We use 6×10^{-5} Pa.s for the CO_2 viscosity. The fluids properties used in the case study are summarized in Table 2. As CO_2 is under a supercritical state and reservoir pressure and temperature conditions are known, we have chosen to fix the CO_2 properties and not estimate them. Otherwise, sensitivity tests have been carried out to estimate CO_2 properties in addition to saturation (Dupuy et al. 2017). The tests show that the CO_2 saturation estimates are only slightly affected if CO_2 properties are unknown.

Sensitivity tests

Sensitivity tests for baseline parameters, i.e. porosity and rock frame moduli before CO_2 injection are carried out. The forward model is based on the extended Biot-Gassmann theory with fully brine saturated Utsira sandstone and is described in the previous part. The grain and frame properties for Utsira sandstone and brine properties are given in Table 1 and 2.

Figure 2 (bottom panel) shows a point test where we estimate frame bulk modulus, frame shear modulus and porosity using a different combination of input data (P-, S-wave velocity and density). Examining the size and the shape of the low misfit area in these sensitivity plots allows assessing the uncertainty of each parameter estimate and how well these estimates are constrained depending on which input data are used. Such extensive sensitivity tests are described in details in Dupuy et al. (2016). In Figure 2, the low misfit area (pink models) is wider when only P-wave velocity is used than when P-, S-wave velocities, and density are input data. The dry shear modulus is a lot better constrained when using V_P, V_S and ρ inputs but

porosity and dry bulk modulus have similar uncertainty. It is also worth noting that mean values of all low misfit models (pink models) are quite close to the true value, even when only P-wave velocity is used. This is a promising conclusion our real data application where acoustic FWI is used to derive P-wave velocity maps.

Similar sensitivity tests are given for CO_2 saturation and Brie exponent estimates in Figure 3. We observe that the CO_2 saturation is correctly estimated when the saturation is low while it is more difficult to get an accurate estimate when CO_2 saturation is high. This effect is directly related to the shape of the V_P-S_{CO2} curve (Figure 1) where we have a quick drop of V_P as soon as little CO_2 is present in the porous medium (fizz-gas effect). However, for Brie exponent larger than 5 (fluid mixture is becoming more and more homogeneous), a change of CO_2 saturation is not affecting P-wave velocity when this saturation is greater than 30-50%. The inversion is consequently more difficult to constrain for high CO_2 saturations and the related uncertainty is larger. It is worth noting that this sensitivity test is carried out using V_P input only. Supplementary tests show that using additional input help to mitigate this issue of non-linearity (Dupuy et al. 2017). This first test was assuming that the fluid mixing law is known (Brie exponent equal to 5). If this patchiness exponent is inverted together with CO_2 saturation (bottom panel of Figure 3), we observe a trade-off between these two parameters which is expected as only P-wave velocity is used as input. The uncertainty of the saturation estimates is consequently larger.

Sleipner test case

The two-step workflow is carried out for data before (1994 vintage, baseline) and after CO_2 injection (2008 vintage, monitor). For both vintages, data corresponding to the inline 1836 is oriented north to south and located close to the injection point are selected. The applied processing workflow aims at improving the signal to noise ratio and without affecting the

amplitudes of the data. It includes the removal of the t^2 divergence compensation, data muting before the first arrivals, and the selection of data with an offset higher than 420 m. The available data include offsets up to 1800 m. For the initial velocity model, we assume a horizontal sea bottom and use a stacking velocity model converted to interval velocity in depth and smoothed. The model is 7 km long and has a depth of 1.35 km. It is defined on a regular 3m squared grid to ensure sufficient accuracy when high frequencies are considered. To mitigate the non-linearity of FWI, we perform the inversion from low to high frequencies using frequency components up to 33 Hz to derive a highly-resolved P-wave velocity model. A target region around the Utsira sandstone is then used as input to perform RPI.

FWI results

Figure 4.a and 4.b show the P-wave velocity maps derived by FWI for both baseline and monitor cases, respectively. Selected interpreted horizons (corresponding to the seabed, the top Pliocene, the intra Pliocene, the top of Utsira sand wedge, the top of Utsira, and the base of Utsira) are also plotted for reference. The top of Utsira sand wedge is an eastward thickening package, which is separated from the main sand part by a shale layer (Zweigel et al. 2004). As observed in Romdhane and Querendez (2014) using a different inline, the models derived from FWI show a clear improvement in term of resolution. Figure 4.b shows clear indications about the lateral extent and geometry of the CO_2 plume. Figure 4.c shows the corresponding time migrated section converted to depth using a simple time to depth relationship based on well data situated at around 800 m distance from the 2D line used. The pushdown of the reflection beneath the CO_2 plume is clearly visible.

Close up of the target region at the depth of Utsira reservoir where the CO_2 is expected to accumulate are shown in Figure 4.d, and 4.e with interpreted horizons corresponding to the top of Utsira sand wedge, the top of Utsira, and to the base of Utsira from top to bottom. For the

baseline case, two thick low-velocity layers can be observed. These layers are probably showing high porosity unconsolidated sandstones where the CO_2 is expected to migrate after injection. For the monitor case, we observe thin low velocity layers that can be associated with the accumulation of CO_2. The velocity pushdown effect at the base of the Utsira can also be observed. The better resolution of the shale-sand interlayers is probably related to the higher contrast between the slow-velocity CO_2 plume and the surrounded high-velocity brine-saturated reservoir, shale overburden and interbedded layers. It is worth noting that the velocities of the overburden layers (just above Utsira reservoir) are slightly lower in the monitor case, while no effect related to CO_2 anomaly should be observed. In addition, velocity differences observed below the reservoir are not meaningful of any physical change because CO_2 migration is driven by buoyancy effect. These uncertainties in velocity can be partly due to some smearing effects (Romdhane et al. 2014, Queiber and Singh 2013) which can lead to overestimation of velocities in the CO_2 plume (i.e. underestimation of velocity change) observed in Utsira sandstone, and to the limited available offset range (maximum of 1800 m).

Baseline dataset: estimation of rock frame properties

We apply the rock physics inversion on baseline data considering that the porous medium is saturated with brine. Similarly to other real case studies (for example, the gas blowout in the North Sea presented by (Dupuy et al. 2016)), prior geological information is helpful to constrain the estimation of rock frame properties. The RPI is applied to the FWI-derived P-wave velocity model to estimate rock frame moduli (K_d, G_d) and porosity φ for the reservoir where the CO_2 plume is expected to accumulate. The inversion ranges are given as: 0.1 GPa < K_d < 10 GPa, 0.01 GPa < G_d < 10 GPa, 0 < φ < 0.45. The inversion frequency is 30 Hz.

The estimated bulk frame modulus, shear frame modulus and porosity and associated uncertainties are given in Figure 5 and Figure 6. The bulk and shear frame moduli within the

two low-velocity sand layers vary from 1 to 3 GPa with $\pm$ 1 to 1.5 GPa uncertainty and from 1 to 1.5 GPa with $\pm$ 0.9 to 1.2 GPa uncertainties, respectively. The surrounding layers (interpreted as being thin shale interbedded layers and the overburden layers) show higher values for both moduli (3 to 6 GPa with $\pm$ 1.5 to 2.5 GPa for the bulk modulus and 2 to 2.5 GPa with $\pm$ 1.15 to 1.5 GPa for the shear modulus). The porosity varies from 0.30 to 0.35 with $\pm$ 0.05 to 0.075 uncertainty in the sands, while it shows lower values in the surrounding layers (0.20 to 0.25 with $\pm$ 0.075 to 0.10 uncertainty). It is worth noting that we can observe the imprint of the a priori parameters (grain density, grain bulk moduli, and permeability) on the porosity map (Figure 5). It is also noticed that the high porosity layers are slightly shifted compared to the interpreted layers. This can be caused by a partially erroneous time to depth conversion of interpreted horizons and related to the smearing effect observed in FWI results. However, knowing that expected resolution of FWI is around half a wavelength which corresponds to approximately 30 m for a frequency of 33 Hz and a velocity of 2000 m/s, this depth mismatch of 10 m maximum is in the range of uncertainty. That's why we chose to not do any stretch matching of these horizons.

Monitor dataset: estimation of CO_2 saturation and patchiness exponent

After the estimation of rock frame properties, we focus on the 2008 vintage dataset for the target region. Figure 7 shows the maps of CO_2 saturation using Brie rock physics model with two exponent values (e=1 and e=5), and when e is inverted together with saturation. Figure 8 shows the associated uncertainties of CO_2 saturation for the three cases. Figure 9 shows the estimation of patchiness exponent and its associated uncertainty for the third case (joint inversion of CO_2 saturation and Brie exponent). The estimation of CO_2 saturation using e=1 (so-called patchy mixing) shows clear CO_2-brine saturated regions, mainly around 880-970 m deep with

saturations reaching 0.90 ± 0.15 to 0.17 uncertainty. The estimations of CO_2 saturation within deeper sandstone layers are lower than 0.50 with ± 0.12 to 0.17 uncertainty.

The estimation of CO_2 saturation using exponent e=5 also shows one high CO_2-brine saturated region (870-970 m deep). CO_2 saturation in this layer varies from 0.30 to 0.70 with ± 0.15 to 0.17 uncertainty. Especially, the highest uncertainty tends to be associated with the highest CO_2 saturated regions. For example, at 910-940 m deep, the CO_2 saturation is going up to 0.70 with ± 0.17 uncertainty. We can also see this distinct high CO_2 saturated region at the depth of approximately 900 m when we invert for the Brie (or patchiness) exponent and CO_2 saturation simultaneously. In this case, the CO_2 saturation is reaching 0.50 in this main layer with an uncertainty around 0.22 to 0.25. The estimations of CO_2 saturations within the deeper sandstone layers vary in the range of 0.20 to 0.30 with ± 0.13 to 0.17 uncertainty. It is worth noting that uncertainties related to CO_2 saturation estimates are higher in this third case, up to 0.25 instead of 0.17 in the two first cases. The patchiness exponent e within these CO_2-brine saturated layers is ranging from 4 to 33 with an uncertainty around 5 to 11. Again, the higher uncertainty in CO_2 saturation tends to be associated with the high CO_2 saturated regions. While lower uncertainty and higher value in the estimation of the patchiness exponent tend to be associated with the high CO_2 saturated regions. For example, the estimations of patchiness exponent vary in the range of 31-36 with ± 5 uncertainty at depth of 910-940 m where the CO_2 saturation is reaching 0.50. High CO_2 saturation and uniform mixing tend to happen at the same location.

It is worth noting that there are large CO_2 saturations above the top Utsira in Figure 7, especially for the case where Brie exponent is equal to 1 (top panel). This feature in overburden should not be interpreted as leaking CO_2. It is linked to the low velocity patch (blue colors) observed in Figure 4.e. It is important to note that this high saturation value is only visible for the patchy saturation case (e=1) and that the results of CO_2 saturation estimates are affected by

uncertainties both related to the first (FWI) and second inversion steps (RPI). The FWI step is dependent on data quality which is different for the baseline (1994 vintage) and monitor (2008 vintage) datasets, making any quantification of 4D changes difficult. For this reason, we opted for a parallel time-lapse FWI strategy. The baseline data is used in our case to derive constraints on rock frame properties in the reservoir. Smearing effect in FWI results can also be a source of "ghost" changes above and below the reservoir as noticed in Figure 4. In addition, the overburden shales have low porosity (<20%) and complex mineralogy, so additional caution must be considered when looking at CO_2 saturations in the overburden because of greater uncertainties in a priori constraints. Finally, Biot-Gassmann theory combined with the effective fluid phase rock physics model have been shown to be relevant for fluid substitution in brine-CO_2 sands but its applicability for shales is less straightforward (Dupuy et al. 2017, Falcon-Suarez et al. 2018, Bergmann and Chadwick 2015, Queiber and Singh 2013). High CO_2 saturation estimates in the overburden are consequently not reliable and no conclusion of any leaking CO_2 should be derived from this result.

Figure 10 shows the 1D profiles of CO_2 saturation and patchiness exponent for the different test cases. The profile is extracted at an offset of 3240 m going through the high CO_2 saturation zone. The main CO_2–brine saturated layers appear between 900 and 950 m deep with CO_2 saturation ranging from 0.60 to 0.90. It is interesting that both patchy mixing (e=1 or e=5 depending on authors) and uniform mixing (e=40) models show CO_2 saturations reaching 0.90. The CO_2 saturation increases when the patchiness exponent decreases, which is directly related to the shape of the velocity versus saturation curves (Figure 1). It is worth noting that the results for exponent equal to 1 are enveloping the other results showing more high-resolution variations. When we invert patchiness exponent and CO_2 saturation at the same time, we observe more oscillations due to the under-determined inversion system. The uncertainty for the estimation of CO_2 saturation varies in the range of $\pm$ 0.12 to 0.17, when we are using a known Brie

exponent. When we invert the CO_2 saturation and the patchiness exponent together, the associated uncertainty of CO_2 saturation goes up to $\pm$ 0.25.

Discussion

In our study, FWI has been used to derive velocity models from both the baseline and monitor datasets and were used as input to infer rock physics properties. The inversion of the monitor dataset provided clear indications about the geometry and lateral extent of the CO_2 plume with the lowest P-wave velocities being in the uppermost layers. We used a parallel time-lapse strategy where models from velocity analysis were used as initial models for the inversion. Alternative strategies (Asnaashari et al. 2015), including the use of a sequential time-lapse inversion and the introduction of a priori information (for example about the overburden), can contribute to the improvement of the derived models.

The values of CO_2 saturation obtained for inline 1836 are higher than those obtained in Dupuy et al. (2017). The inline data used in our study is located very close to the injection point, while the 1D section shown in Dupuy et al. (2017) is located approximately 500 m away from the injection point. For comparison, Queiber and Singh (2013) get values up to 0.90 using 2006 vintage, while Golding et al. (2011) suggest that saturation is probably higher than 0.30. Recent work by Ghosh et al. (2015) gives estimations between 0.20 and 0.80 depending on the mixture type (patchiness exponent). In previous tests using the same methodology shown by Dupuy et al. (2017), rock frame properties are derived from well-log data acquired at the injection well. The effect of a priori properties (i.e., rock frame, grains and fluid parameters) on CO_2 saturation estimates can strongly affect the results, and these a priori parameters should be handled with care. Estimating them from baseline data can be a better solution. It is anyway worth keeping in mind that uncertainty related to baseline estimates (bulk and shear moduli as well as porosity)

is not negligible and is a key factor in the CO_2 saturation quantification. Even if our sensitivity tests show that the mean values of these baseline properties estimated from P-wave velocity only are close to the true value, uncertainty is not negligible and other sensitivity tests show that the CO_2 saturation can be changed by 0.10 to 0.20 if the baseline properties are different.

Regarding the mixture distribution, Sen et al. (2016) use a capillary pressure equilibrium theory and show that the CO_2 distribution at Sleipner is more uniform for high CO_2 saturation and more patchy for low CO_2 saturation. We found similar trends in our results. For example, the patchiness exponent is higher for the highly CO_2 saturated layers, which is indicating a more uniform mixing while the patchiness exponent is smaller for the less CO_2 saturated layers. Ghosh et al. (2015) also found that the CO_2 phase is not fully patchy or uniformly saturated in the reservoir. Zhang et al. (2014) and Chadwick et al. (2010) propose an approach using history-matching simulations and 4D seismic data. They get a higher estimation of CO_2 saturation with some values up to 0.98. In our study, the highly saturated layers show saturations varying between 0.60 and 0.90 with an uncertainty of 0.12 to 0.20. Lumley et al. (2008) suggest that it is difficult to quantify the CO_2 saturation when it is larger than 0.30. In our study, we also observe that the estimated uncertainty is higher for higher CO_2 saturation (Figure 1 and 3). Relevant uncertainty assessment and quantification still need to be carried out. Proper uncertainty propagation from seismic imaging (using the method suggested in Eliasson and Romdhane (2017) for example) to rock physics inversion can be taken into account using a fully Bayesian formulation. More constraints to the inversion process could be added to mitigate the trade-off between saturation and patchiness exponent (standing for the rock physics model itself). For example, using additional inputs from seismic inversion (attenuation, shear wave velocity, AVO attributes) or from other geophysical techniques (gravity, CSEM) can lead to reduce the non-uniqueness of the inversion (Gao et al. 2012, Liang et al. 2016, Subagjo et al. 2018).

Conclusions

We derive a quantitative spatial distribution of CO_2 saturation through the combination of FWI and RPI. The two-step workflow is applied to a selected inline from both baseline and monitor surveys at Sleipner. We first estimate rock frame properties based on baseline data which are then used as an input to the monitor vintage study. We found that CO_2 saturations can reach 0.60 to 0.90 ± 0.12 to 0.25 near the injection point when the patchiness exponent is assumed to be known. The uncertainty of the CO_2 saturation estimation is relatively low for most cases but tends to increase for higher CO_2 saturations. We show the possibility to estimate the CO_2-brine mixture law by estimating the patchiness exponent and CO_2 saturation simultaneously. The patchiness exponent is globally varying from 5 to 33 which indicates a distribution of CO_2 and brine between fully patchy (e=1) and fully uniform (e=40) mixings. But it tends to be a very uniform mixing when CO_2 saturation is very high.

Acknowledgements

This publication has been produced with support from the NCCS Centre, performed under the Norwegian research program Centres for Environment-friendly Energy Research (FME). The authors acknowledge the following partners for their contributions: Aker Solutions, ANSALDO Energia, CoorsTek Membrane Sciences, Gassco, KROHNE, Larvik Shipping, Norcem, Norwegian Oil and Gas, Quad Geometrics, Shell, Statoil, TOTAL, and the Research Council of Norway (257579/E20). We thank also the uniCQue KPN project (233716/E20). We also thank Malcolm Sambridge for providing NA software and Statoil for sharing Sleipner dataset.

References

Adler, P.M., Jacquin, C.G. & Thovert, J.F. 1992. The formation factor of reconstructed porous media. *Water Resources Research* **28**, 1571-1576.

Arts, R., Chadwick, A., Eiken, O., Thibeau, S. & Nooner, S. 2008. Ten years' experience of monitoring CO2 injection in the Utsira Sand at Sleipner, offshore Norway. *First break* **26**.

Arts, R., Eiken, O., Chadwick, A., Zweigel, P., Van der Meer, L. & Zinszner, B. 2004. Monitoring of CO 2 injected at Sleipner using time-lapse seismic data. *Energy* **29**, 1383-1392.

Arts, R., Elsayed, R., Van Der Meer, L., Eiken, O., Ostmo, S., Chadwick, A., Kirby, G. & Zinszner, B. Year. Estimation of the mass of injected CO2 at Sleipner using time-lapse seismic data. Conference Estimation of the mass of injected CO2 at Sleipner using time-lapse seismic data.

Asnaashari, A., Brossier, R., Garambois, S., Audebert, F., Thore, P. & Virieux, J. 2015. Time-lapse seismic imaging using regularized full-waveform inversion with a prior model: which strategy? *Geophysical Prospecting* **63**, 78-98.

Bergmann, P. & Chadwick, A. 2015. Volumetric bounds on subsurface fluid substitution using 4D seismic time shifts with an application at Sleipner, North Sea. *Geophysics* **80**, B153-B165.

Biot, M.A. 1956a. Theory of propagation of elastic waves in a fluid-saturated porous solid. I. Low-frequency range. *The Journal of the acoustical Society of america* **28**, 168-178.

Biot, M.A. 1956b. Theory of propagation of elastic waves in a fluid-saturated porous solid. II. Higher frequency range. *The Journal of the acoustical Society of america* **28**, 179-191.

Boait, F., White, N., Bickle, M., Chadwick, R., Neufeld, J. & Huppert, H. 2012. Spatial and temporal evolution of injected CO2 at the Sleipner Field, North Sea. *Journal of Geophysical Research: Solid Earth* **117**.

Böhm, G., Carcione, J.M., Gei, D., Picotti, S. & Michelini, A. 2015. Cross-well seismic and electromagnetic tomography for CO2 detection and monitoring in a saline aquifer. *Journal of Petroleum Science and Engineering* **133**, 245-257.

Brie, A., Pampuri, F., Marsala, A. & Meazza, O. Year. Shear sonic interpretation in gas-bearing sands. Conference Shear sonic interpretation in gas-bearing sands.

Carcione, J.M. & Picotti, S. 2006. P-wave seismic attenuation by slow-wave diffusion: Effects of inhomogeneous rock properties. *Geophysics* **71**, O1-O8.

Chadwick, A., Williams, G., Delepine, N., Clochard, V., Labat, K., Sturton, S., Buddensiek, M.-L., Dillen, M., Nickel, M. & Lima, A.L. 2010. Quantitative analysis of time-lapse seismic monitoring data at the Sleipner CO2 storage operation. *The Leading Edge*.

Chadwick, R., Holloway, S., Kirby, G., Gregersen, U. & Johannessen, P. Year. The Utsira Sand, Central North Sea–an assessment of its potential for regional CO2 disposal. Conference The Utsira Sand, Central North Sea–an assessment of its potential for regional CO2 disposal, 349-354.

Chadwick, R., Zweigel, P., Gregersen, U., Kirby, G., Holloway, S. & Johannessen, P. 2004. Geological reservoir characterization of a CO2 storage site: the Utsira Sand, Sleipner, northern North Sea. *Energy* **29**, 1371-1381.

Dupuy, B., Garambois, S. & Virieux, J. 2016. Estimation of rock physics properties from seismic attributes — Part 1: Strategy and sensitivity analysis. *Geophysics* **81**, M35-M53.

Dupuy, B., Romdhane, A., Eliasson, P., Querendez, E., Yan, H., Torres, V.A. & Ghaderi, A. 2017. Quantitative seismic characterization of CO2 at the Sleipner storage site, North Sea. *Interpretation* **5**, SS23-SS42.

Dupuy, B. & Stovas, A. 2016. Effect of anelastic patchy saturated sand layers on the reflection and transmission responses of a periodically layered medium. *Geophysical Prospecting* **64**, 299-319.

Eiken, O., Brevik, I., Arts, R., Lindeberg, E. & Fagervik, K. 2000. Seismic monitoring of CO2 injected into a marine acquifer. In: *SEG Technical Program Expanded Abstracts 2000*, pp. 1623-1626. Society of Exploration Geophysicists, ISBN 1052-3812.

Eliasson, P. & Romdhane, A. 2017. Uncertainty quantification in waveform-based imaging methods-a Sleipner CO2 monitoring study. *Energy Procedia* **114**, 3905-3915.

Falcon-Suarez, I., Papageorgiou, G., Chadwick, A., North, L., Best, A.I. & Chapman, M. 2018. CO2-brine flow-through on an Utsira Sand core sample: Experimental and modelling. Implications for the Sleipner storage field. *International Journal of Greenhouse Gas Control* **68**, 236-246.

Furre, A.-K., Eiken, O., Alnes, H., Vevatne, J.N. & Fredrik, A. 2017. 20 years of monitoring CO2-injection at Sleipner.

Furre, A.-K., Kiær, A. & Eiken, O. 2015. CO2-induced seismic time shifts at Sleipner. *Interpretation* **3**, SS23-SS35.

Furre, A.K. & Eiken, O. 2014. Dual sensor streamer technology used in Sleipner CO2 injection monitoring. *Geophysical Prospecting* **62**, 1075-1088.

Gao, G., Abubakar, A. & Habashy, T.M. 2012. Joint petrophysical inversion of electromagnetic and full-waveform seismic data. *Geophysics* **77**, WA3-WA18.

Gasda, S., Nilsen, H. & Dahle, H. Year. Upscaled models for CO2 migration in geological formations with structural heterogeneity. Conference Upscaled models for CO2 migration in geological formations with structural heterogeneity.

Gassmann, F. 1951. Uber die elastizitat poroser medien: Verteljahrss-chrift der Naturforschenden Gesellschaft in Zurich, 96, 1–23. *Translated to English in the 16th issue of Geophysics*.

Ghaderi, A. & Landrø, M. 2009. Estimation of thickness and velocity changes of injected carbon dioxide layers from prestack time-lapse seismic data. *Geophysics* **74**, O17-O28.

Ghosh, R., Sen, M.K. & Vedanti, N. 2015. Quantitative interpretation of CO2 plume from Sleipner (North Sea), using post-stack inversion and rock physics modeling. *International Journal of Greenhouse Gas Control* **32**, 147-158.

Golding, M.J., Neufeld, J.A., Hesse, M.A. & Huppert, H.E. 2011. Two-phase gravity currents in porous media. *Journal of fluid mechanics* **678**, 248-270.

Halland, E.K., Gjeldvik, I., Johansen, W., Magnus, C., Meling, I., Pedersen, S., Riis, F., Solbakk, T. & Tappel, I. 2011. CO2 Storage Atlas Norwegian North Sea. *Norwegian Petroleum Directorate, PO Box* **600**.

Hashin, Z. & Shtrikman, S. 1963. A variational approach to the theory of the elastic behaviour of multiphase materials. *Journal of the Mechanics and Physics of Solids* **11**, 127-140.

Hustedt, B., Operto, S. & Virieux, J. 2004. Mixed-grid and staggered-grid finite-difference methods for frequency-domain acoustic wave modelling. *Geophysical Journal International* **157**, 1269-1296.

Johnson, D.L., Koplik, J. & Dashen, R. 1987. Theory of dynamic permeability and tortuosity in fluid-saturated porous media. *Journal of fluid mechanics* **176**, 379-402.

Liang, L., Abubakar, A. & Habashy, T.M. 2016. Reservoir property mapping and monitoring from joint inversion of time-lapse seismic, electromagnetic, and production data. *Geophysics* **81**, ID73-ID84.

Lindeberg, E. 2013. (ed. C. Calculation of thermodynamic properties of CO2, H2O and their mixtures also including salt with the Excel macro ‘‘CO2 Thermodynamics’’.). SINTEF.

Lumley, D., Adams, D., Wright, R., Markus, D. & Cole, S. 2008. Seismic monitoring of CO 2 geo-sequestration: realistic capabilities and limitations. In: *SEG Technical Program Expanded Abstracts 2008*, pp. 2841-2845. Society of Exploration Geophysicists, ISBN 1052-3812.

Mavko, G., Mukerji, T. & Dvorkin, J. 2009. *The rock physics handbook: Tools for seismic analysis of porous media.* Cambridge university press, ISBN 0521861365.

Metz, B., Davidson, O., De Coninck, H., Loos, M. & Meyer, L. 2005. IPCC special report on carbon dioxide capture and storage. Intergovernmental Panel on Climate Change, Geneva (Switzerland). Working Group III.

Michael, K., Golab, A., Shulakova, V., Ennis-King, J., Allinson, G., Sharma, S. & Aiken, T. 2010. Geological storage of CO2 in saline aquifers—a review of the experience from existing storage operations. *International Journal of Greenhouse Gas Control* **4**, 659-667.

Papageorgiou, G., Amalokwu, K. & Chapman, M. 2016. Theoretical derivation of a Brie-like fluid mixing law. *Geophysical Prospecting* **64**, 1048-1053.

Pratt, R.G., Shin, C. & Hick, G. 1998. Gauss–Newton and full Newton methods in frequency–space seismic waveform inversion. *Geophysical Journal International* **133**, 341-362.

Pride, S. 2005. In: *Hydrogeophysics: Water Science and Technology Library: Springer*, pp. 253–284.

Queiber, M. & Singh, S.C. 2013. Full waveform inversion in the time lapse mode applied to CO2 storage at Sleipner. *Geophysical Prospecting* **61**, 537-555.

Romdhane, A. & Querendez, E. 2014. CO2 characterization at the Sleipner field with full waveform inversion: Application to synthetic and real data. *Energy Procedia* **63**, 4358-4365.

Romdhane, A., Querendez, E. & Ravaut, C. 2014. CO2 Thin-layer Detection at the Sleipner Field with Full Waveform Inversion: Application to Synthetic and Real Data. *Energy Procedia* **51**, 281-288.

Sambridge, M. 1999. Geophysical inversion with a neighbourhood algorithmöII. Appraising the ensemble. *Geophys. J. Int* **138**, 727-746.

Sen, A., Ghosh, R. & Vedanti, N. 2016. Saturation estimation from 4D seismic data from Sleipner Field by a capillary pressure-based rock-physics model. In: *SEG Technical Program Expanded Abstracts 2016*, pp. 3314-3321. Society of Exploration Geophysicists, ISBN 1949-4645.

Singh, V.P., Cavanagh, A., Hansen, H., Nazarian, B., Iding, M. & Ringrose, P.S. Year. Reservoir modeling of CO2 plume behavior calibrated against monitoring data from Sleipner, Norway. Conference Reservoir modeling of CO2 plume behavior calibrated against monitoring data from Sleipner, Norway.

Subagjo, I., Dupuy, B., Park, J., Romdhane, A., Querendez, E. & Stovas, A. Year. Joint rock physics inversion of seismic and electromagnetic data for CO2 monitoring at Sleipner. Conference Joint rock physics inversion of seismic and electromagnetic data for CO2 monitoring at Sleipner, Porto (Portugal).

Teja, A. & Rice, P. 1981. Generalized corresponding states method for the viscosities of liquid mixtures. *Industrial & Engineering Chemistry Fundamentals* **20**, 77-81.

Voigt, W. 1928. Lehrbuch der Kristallphysik (1928). *Teubner, Berlin*, 962.

White, D. 2013. Toward quantitative CO 2 storage estimates from time-lapse 3D seismic travel times: An example from the IEA GHG Weyburn–Midale CO 2 monitoring and storage project. *International Journal of Greenhouse Gas Control* **16**, S95-S102.

Williams, G. & Chadwick, A. 2012. Quantitative seismic analysis of a thin layer of CO 2 in the Sleipner injection plume. *Geophysics* **77**, R245-R256.

Zhang, G., Lu, P. & Zhu, C. 2014. Model predictions via history matching of CO2 plume migration at the Sleipner Project, Norwegian North Sea. *Energy Procedia* **63**, 3000-3011.

Zweigel, P. 2000. Reservoir geology of the storage unit in the Sleipner CO2-injection case. SINTEF.

Zweigel, P., Arts, R., Lothe, A.E. & Lindeberg, E.B. 2004. Reservoir geology of the Utsira Formation at the first industrial-scale underground CO2 storage site (Sleipner area, North Sea). *Geological Society, London, Special Publications* **233**, 165-180.

Figures

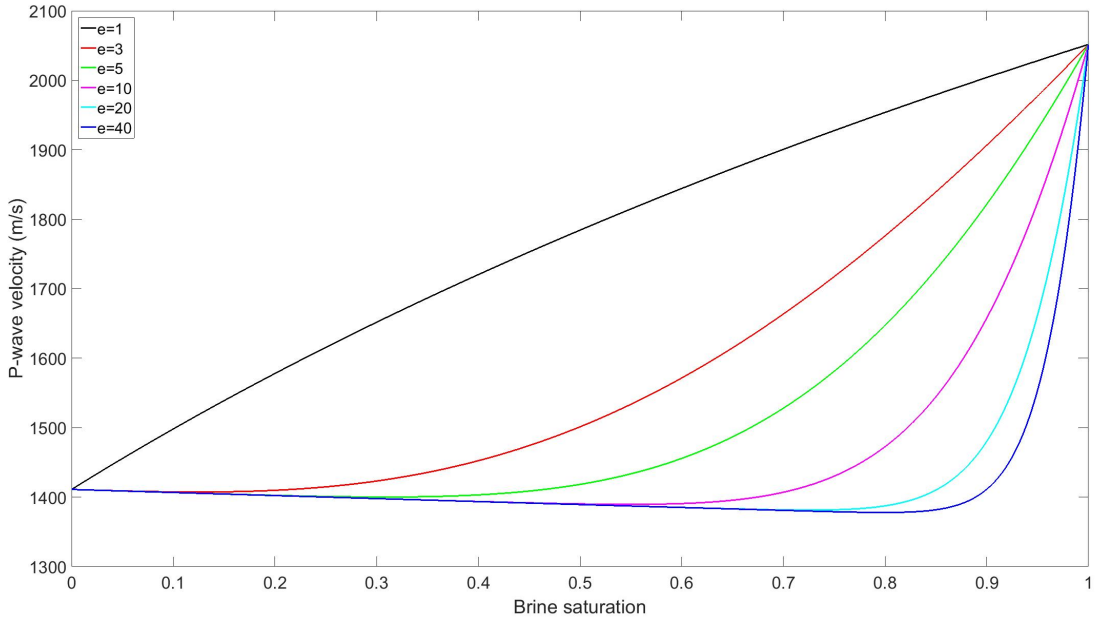

Figure 1 P-wave velocity variation with brine saturation for various patchiness exponents.

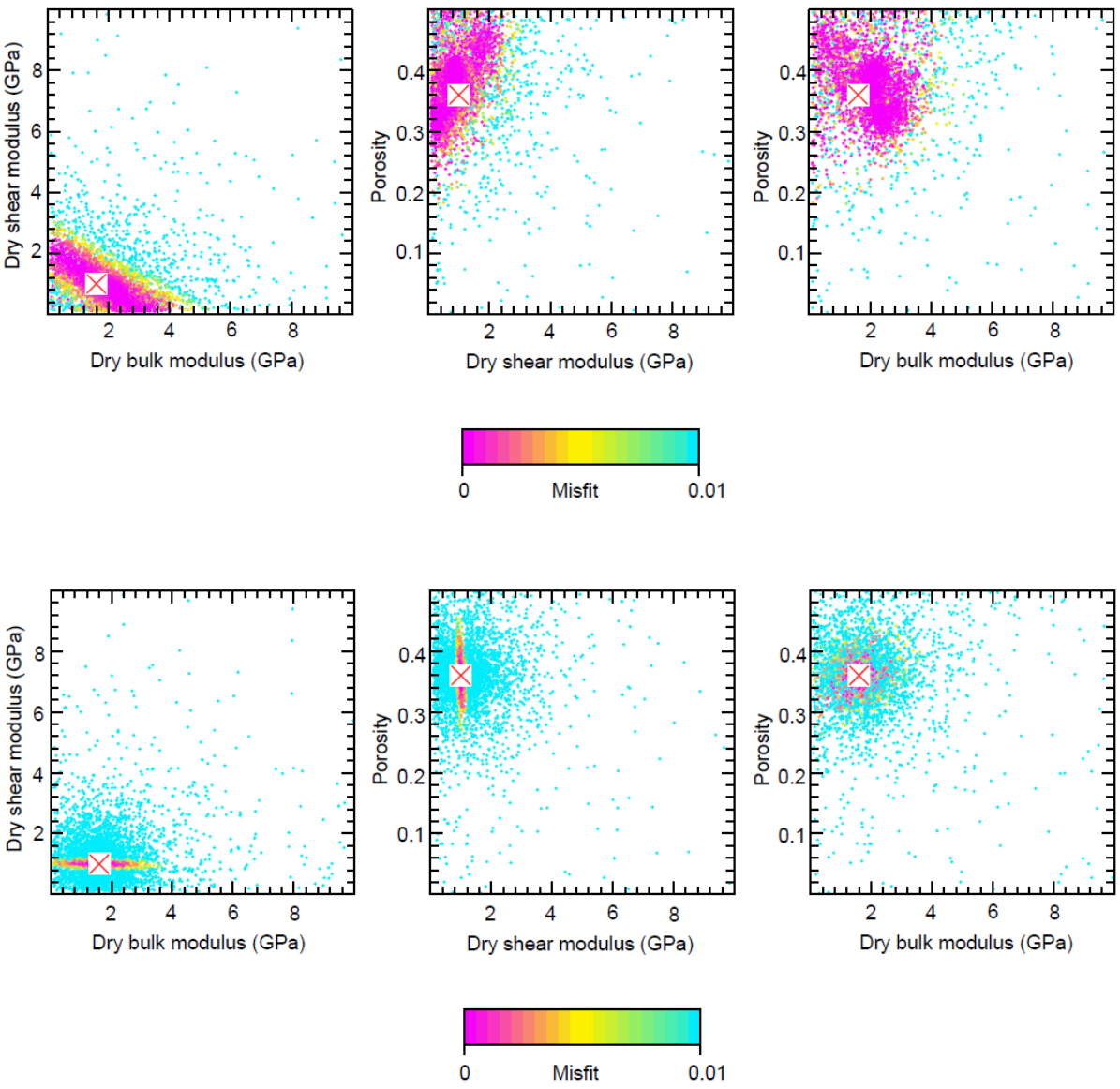

Figure 2 Estimation of dry shear modulus, dry bulk modulus and porosity from P- wave velocity (top panels) and from P-, S-wave velocities and density (bottom panel). The red cross indicates the true model. The color of each dot represents the misfit value for each computed model (between 0 and 0.01).

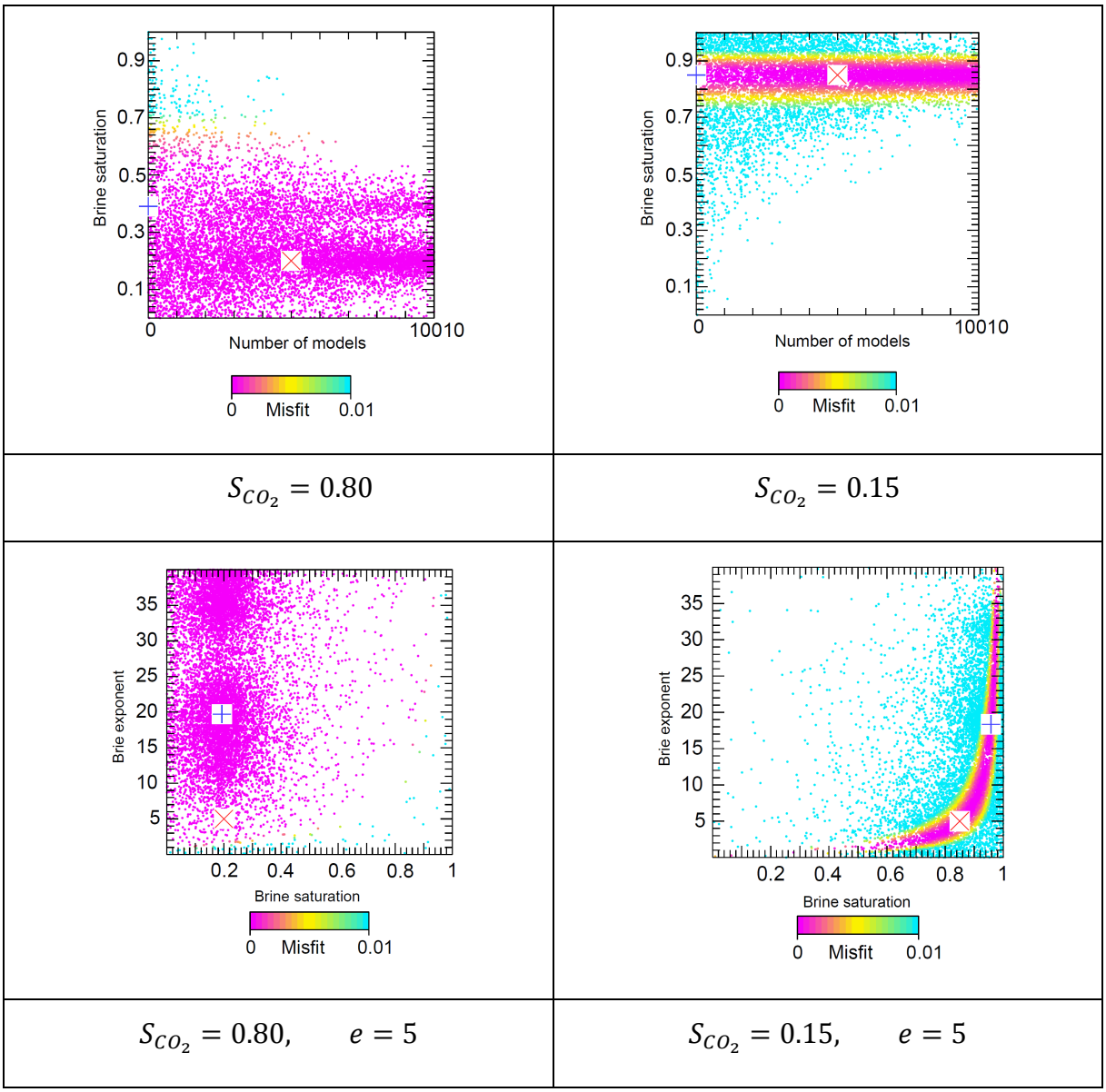

Figure 3 Estimation of brine saturation S_W (top panels) and estimation of brine saturation and patchiness exponent (bottom panels) from P-wave velocity (Figures from (Dupuy et al. 2017)). The blue cross indicates the model with the lowest misfit and the red cross indicates the true model. The color of each dot represents the misfit value for each computed model (between 0 and 0.01; all models with misfit higher than 0.01 are clipped).

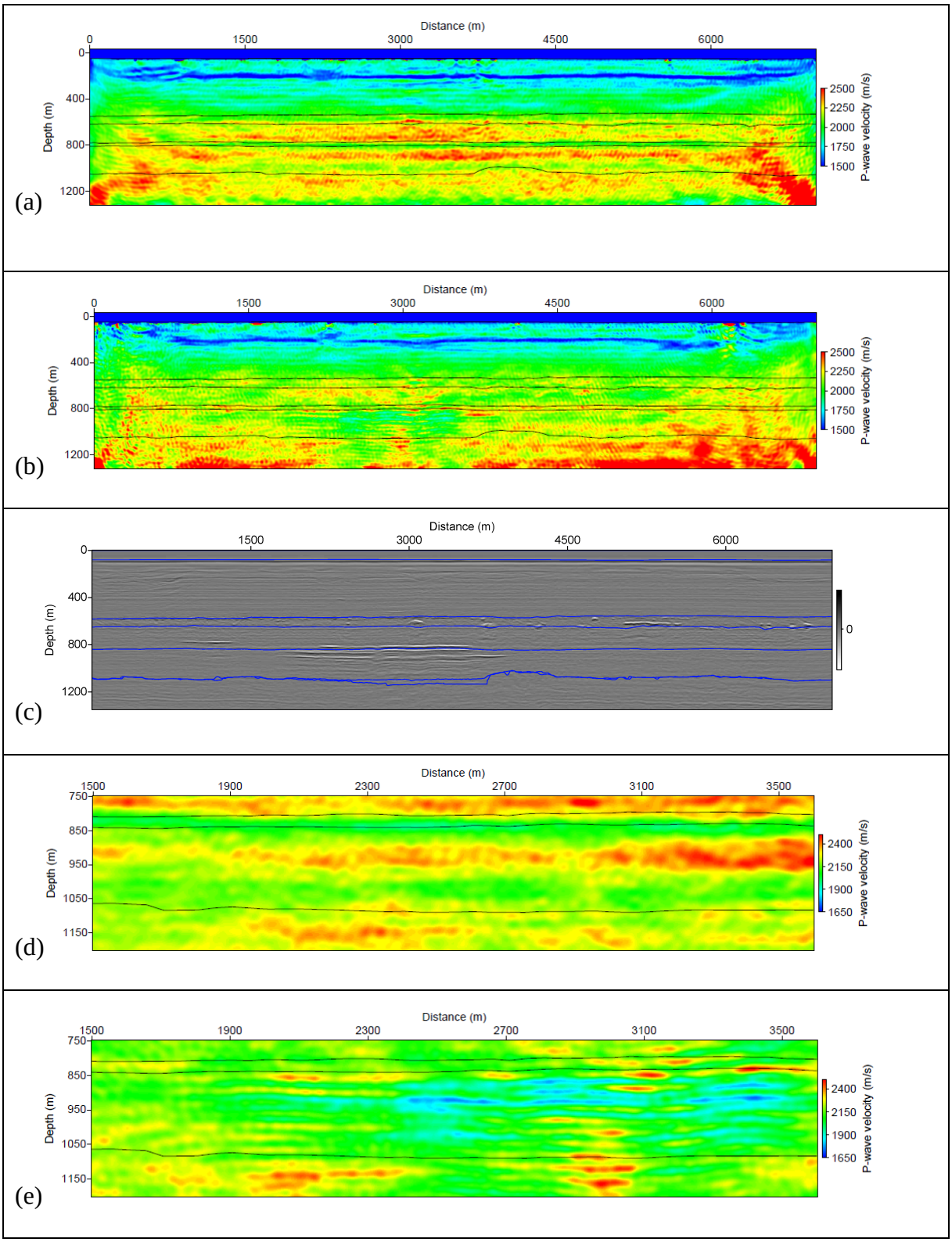

Figure 4 From top to bottom: (a) P-wave velocity model of baseline vintage (1994) derived by FWI, (b) P-wave velocity model of monitor vintage (2008) derived by FWI. (c): Corresponding time migrated section converted to depth. (d, e): Close-ups around the reservoir where CO_2 is

injected for (d) baseline and (e) monitor models. The injection point is located at 1012 m deep. The FWI has been carried out with limited offset (1800 m) with frequencies inverted up to 33 Hz. The black (and blue lines in (c)) correspond to selected interpreted horizons. For the full sections (three top figures), the black lines are indicating the seabed, the top Pliocene, the intra Pliocene, the top of Utsira sand wedge, the top of Utsira and the base of Utsira from top to bottom. For the close-up sections (two bottom figures), the black lines are indicating the top of Utsira sand wedge, the top of Utsira and the base of Utsira from top to bottom. The base of the Utsira is added to (c).

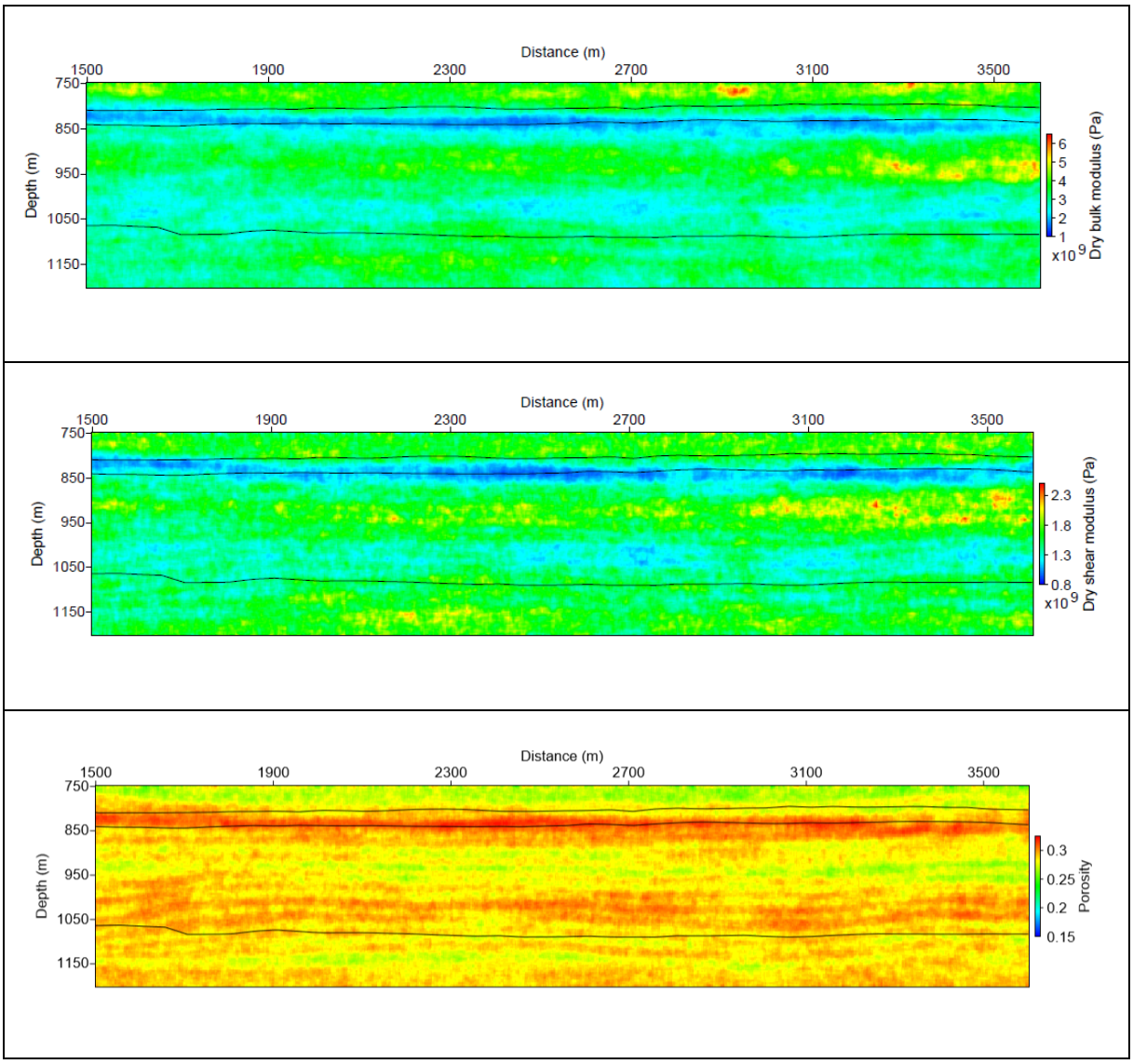

Figure 5 From top to bottom: frame bulk modulus K_d, frame shear modulus G_d and porosity φ. The black lines are figuring the interpreted horizons, i.e. the top of Utsira sand wedge, the top of Utsira and the base of Utsira from top to bottom.

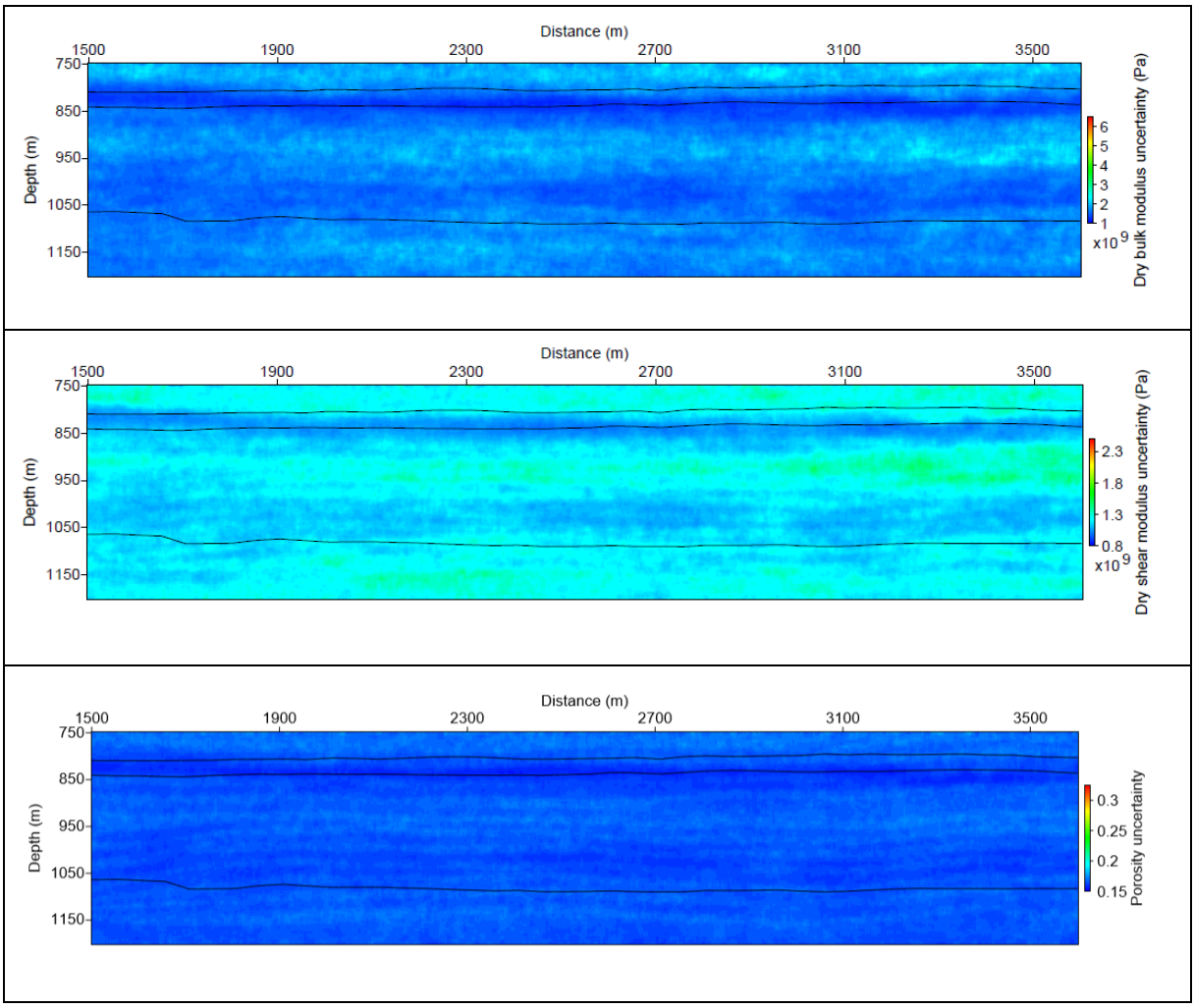

Figure 6 From top to bottom: related uncertainty of frame bulk modulus K_d, frame shear modulus G_d and porosity φ. The black lines are figuring the interpreted horizons, i.e. the top of Utsira sand wedge, the top of Utsira and the base of Utsira from top to bottom.

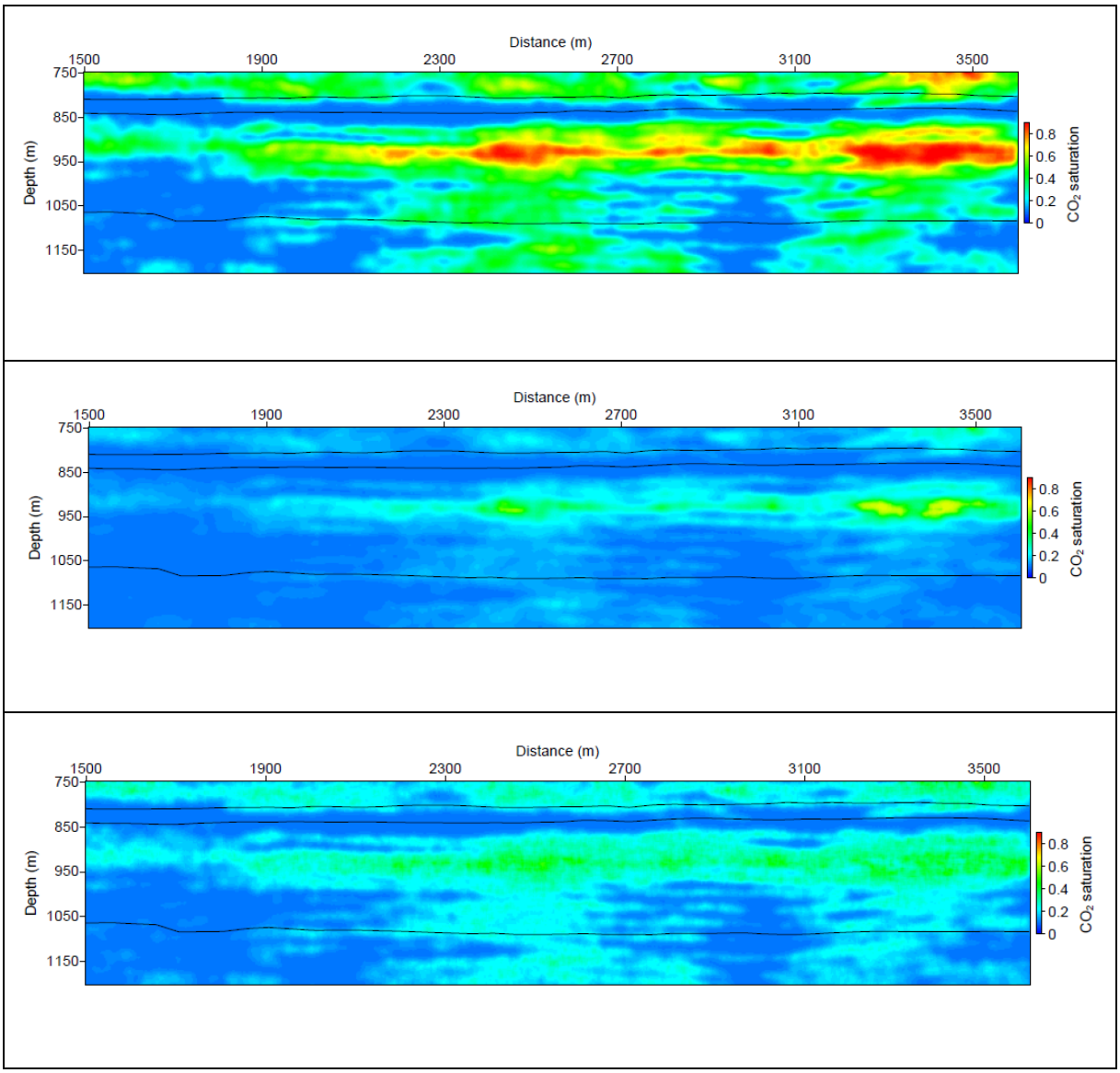

Figure 7 From top to bottom: CO_2 saturation estimated by RPI using patchiness exponent e=1, e=5 and exponent inverted (given in Figure 9).

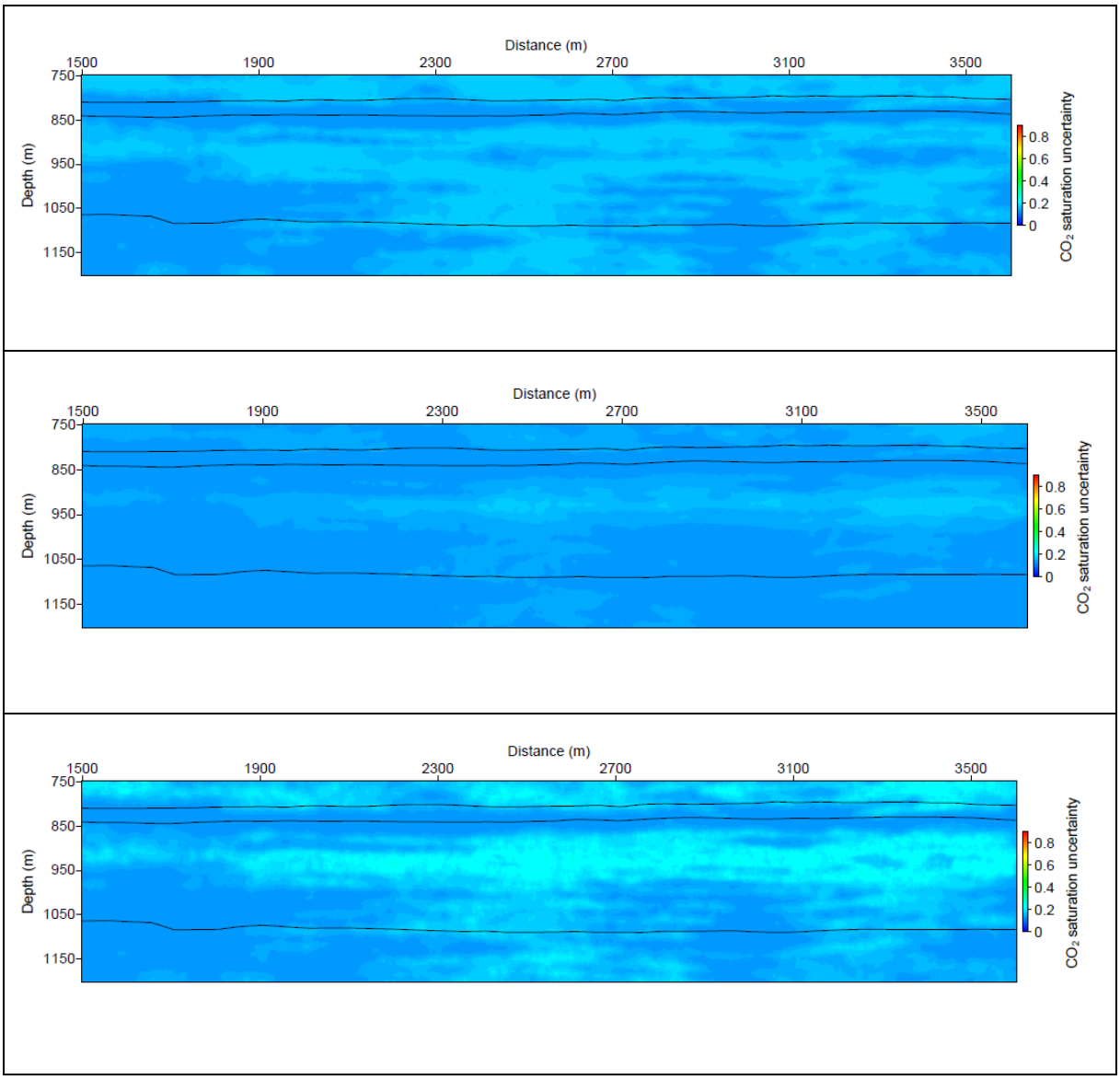

Figure 8 From top to bottom: the uncertainty of CO_2 saturation estimated by RPI using patchiness exponent e=1, e=5 and exponent inverted (given in Figure 9).

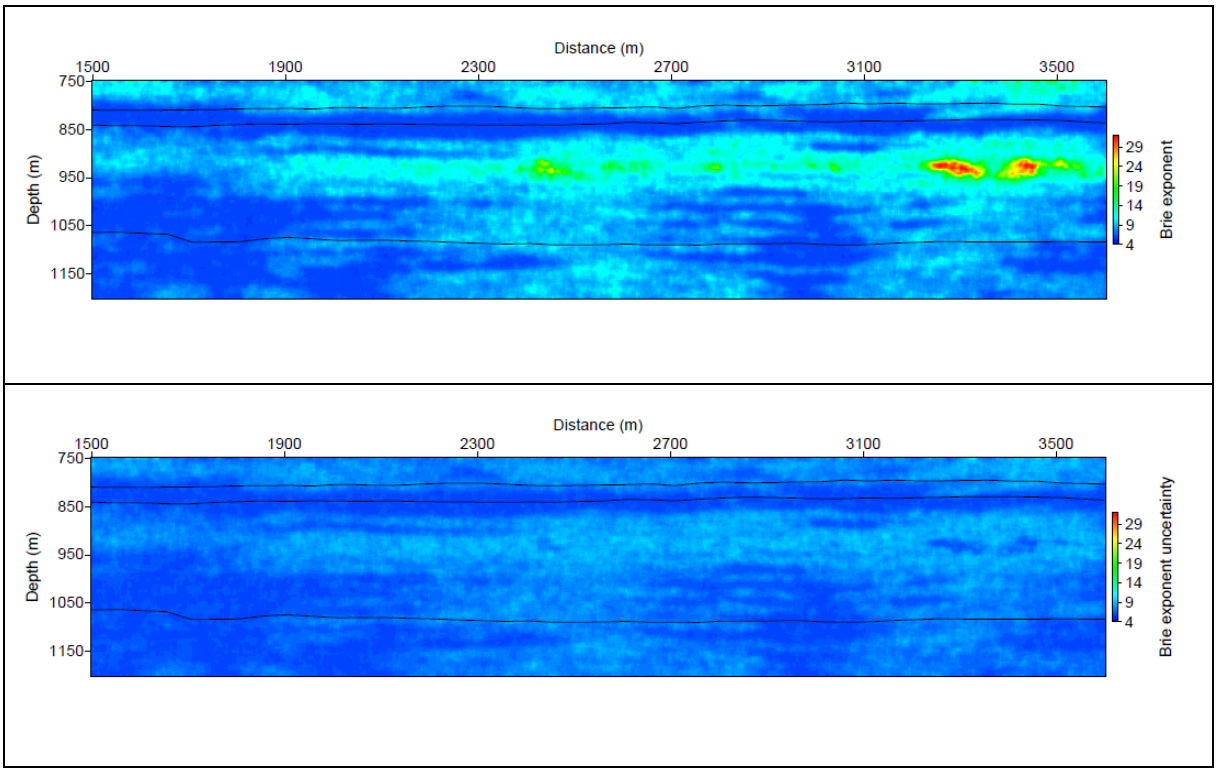

Figure 9 From top to bottom: estimation of patchiness exponent and related uncertainty. The patchiness has been inverted together with CO_2 saturation (given in Figure 7).

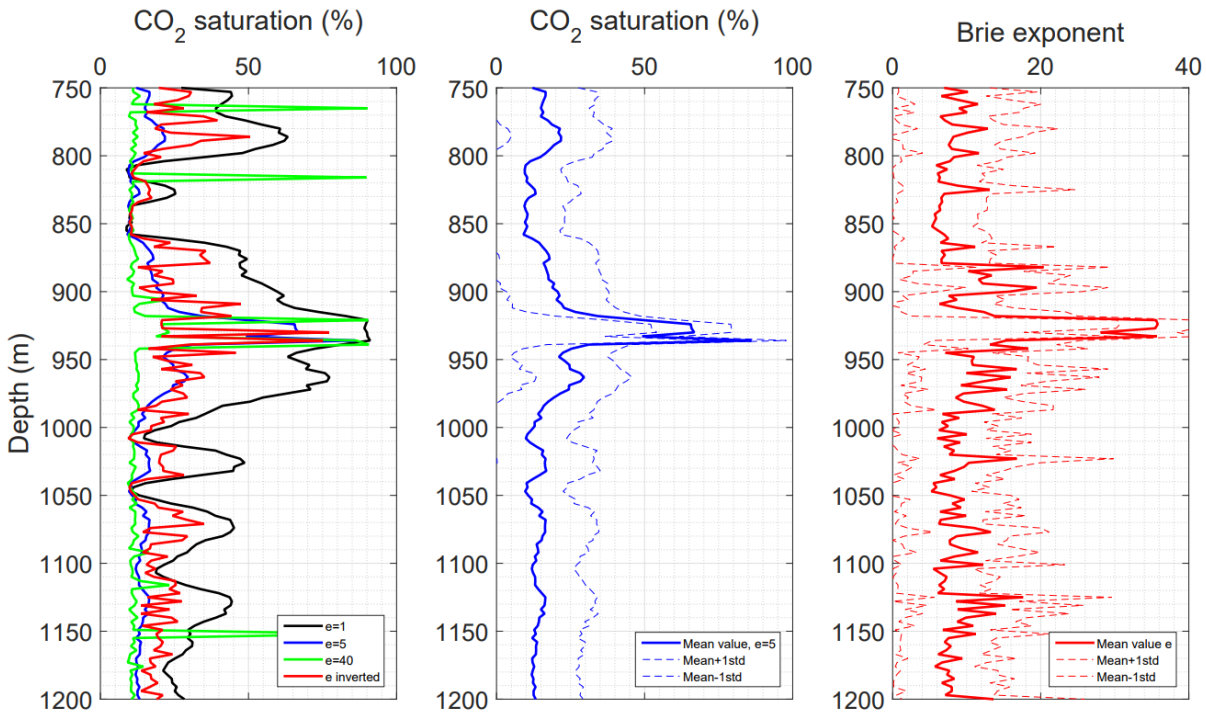

Figure 10 From left to right: 1D profiles of CO_2 saturation estimation using different patchiness exponents, 1D profiles of CO_2 saturation estimation and related uncertainty for e=5 and 1D profiles of patchiness exponent and related uncertainty. The 1D profiles are extracted for an offset equal to 3240 m. The dotted lines correspond to the mean values and the dashed lines stand for the mean value ± one standard deviation.

Tables

Table 1 Utsira sandstone and Nordland shale properties.

Lithology	Grain properties		Rock frame properties	
	K_S	ρ_S	m	k_o
	GPa	kg/m^3		m^2
Utsira Sandstone	39.29	2663.5	1	2×10^{-12}
Nordland Shale	22.6	2390	1	1.48×10^{-17}

Table 2 Brine and CO_2 properties.

Fluid phase	Fluid properties		
	η	ρ_f	K_f
	Pa.s	kg/m^3	GPa
Brine	6.9×10^{-4}	1030	2.3
CO_2	6×10^{-5}	700	0.075